Investigating the structural, optical and electrochemical performance of bismuth ferrite (BiFeO₃) nanoparticles toward photocatalytic activity: as an effect of reducing agent

R. M. Muthukrishnan[1], D. Renuka Devee[2], P. Mohammed Yusuf Ansari[1], T. Sivanesan[2], and S. M. Abdul Kader[1,*] (iD)

[1] Department of Physics, Sadakathullah Appa College (Autonomous), Manonmaniam Sundaranar University, Tirunelveli, Tamil Nadu 627011, India
[2] PG and Research Department of Physics, Pachaiyappa's College, Chennai, Tamil Nadu 600030, India

ABSTRACT

Multifunctional bismuth ferrite (BFO) nanoparticles were successfully synthesized using the co-precipitation technique. pH being a key factor in co-precipitation technique was used to optimize the phase pure synthesis of BFO. The undergone structural changes were examined using XRD. The XRD result shows the distortion in rhombohedral structure of the synthesized sample. Under Ultraviolet-visible spectroscopy, the occurrence of d–d transition and C–T transition taking place in BFO sample was investigated. In addition, the band gap values of BFO1, BFO2 and BFO3 were determined using Tauc's plot and the values are 2.18 eV, 2.18 eV and 2.12eV, respectively. The suppression of modes of vibration in BFO explains the structural distortion caused by reducing agent; these results are consistent with the XRD results. Finally, through electrochemical analysis the redox behavior and the electron hole transport of the samples were analyzed to identify the suitable sample for photocatalytic performance. EIS spectra were carried out to understand the charge transfer resistance of the samples. The electrostatic interaction of catalyst with Fenton reagent and target material was performed at different ranges of pH 3 to 10 which shows enhanced photocatalytic activity toward picric acid (PA).

Address correspondence to E-mail: aksac.physics@gmail.com

Ⓐ Springer

1 Introduction

The rhombohedral distorted perovskite bismuth ferrite (BFO) with ferroelectric (T_c=1103K) and ferromagnetic (T_N = 643K) property offers a magnetoelectric coupling effect (ME) and plays a leading role in the field of multiferroic. In point to practical applications, BFO promises to serve a wide range of applications such as memory devices, sensors, actuators, water splitting, photocatalytic activity and many more [1, 2].

Therefore, over a few decades researchers have adopted various techniques to address the challenge of (i) phase purity, (ii) leakage current and (iii) weak antiferromagnetic properties. But it is still a challenging one. Due to the presence of secondary phases such as $Bi_{25}FeO_{40}$ and $Bi_2Fe_4O_9$, achieving phase purity is a difficult task [3]. In an account with leakage current, the reduction of Fe^{3+} species to Fe^{2+} species creates an oxygen vacancy for charge compensation. This leads to the decrease in electrical resistivity of the material reflecting on the ferromagnetic property of BFO. From our literature survey, we have found that the synthesis of BFO was carried out using various techniques such as solid-state, hydrothermal, sol–gel, co-precipitation, autocombustion, etc. [4–10]. Among these techniques, co-precipitation technique has various control factor like pH, reducing agent, concentration and synthesizing temperature to optimize the compound formation. Therefore, the recent research in understanding the influence of synthesis technique over the property of the material is widely investigated [11].

Allowing various chemical products, particularly nitro compounds, to be disposed of in water poses a risk to human health. 2,4,6-trinitrophenol (PA) is a well-known polynitrated aromatic volatile with explosive materials that has been found to be more lethal than TNT. The ease of solubility of PA in water (12–14 g/L, even at 20 °C) has resulted in a seriously hazardous environmental pollutants [12–14]. Recently, the degradation of organic pollutants has been accomplished using advanced oxidation process (AOP) technology, which completely abates the organic contamination into harmless product, creating the conditions for addressing the aforementioned issues. AOPs in general involve the production of highly reactive hydroxyl (OH) radicals (high oxidation potential, 2.8 eV) that promote complete degradation of organic compounds into innocuous products at high reaction rates [15–19]. Bismuth ferrite ($BiFeO_3$) is the hottest photocatalyst among the perovskites that consumes very less energy with lower band gaps of 2.1 eV and has a larger contact area along with rhombohedral phase, chemically stable with low cost. Furthermore, the piezo-electromagnetic characteristics offer ease degradation while completing the process. Very recently, nanostructured $BiFeO_3$ started to be utilized in the areas of degradation of organic pollutants including dyes, organic pesticides, pharmaceutical wastes and other toxic molecules.

In our present work, we have initially optimized the formation of $BiFeO_3$ through a major factor pH involved in the co-precipitation technique. Phase confirmation was carried using X-ray diffraction technique. Raman spectroscopy discusses the modes of vibration undergone by the samples. UV reveals the excitation of electrons leading totransitions. CV discusses the anomalous behavior of redox reaction as an effect of reducing agents. Further, we have performed a detailed study of degradation of picric acid in UV–visible radiation and solar radiation.

2 Experimental details

The synthesizing materials used in the preparation of $BiFeO_3$ were bismuth nitrate Bi $(NO_3)_3$ 0.5 H_2O(CAS No: 10035-06-0), iron nitrate Fe $(NO_3)_3$ 0.9 H_2O(CAS No: 7782-61-8), ammonia hydroxide NH_4OH(CAS No: 1336-21-6), sodium hydroxide NaOH(CAS No: 1310-73-2), potassium hydroxide KOH(CAS No: 1310-58-3) which are of analytical grade.

Bi $(NO_3)_3.5H_2O$ and Fe $(NO_3)_3.9H_2O$ were used as a precursor and NH_4OH, NaOH and KOH as a mineralizer. Bismuth nitrate (0.1 M) and iron nitrate (0.1 M) were taken in a 1:1 stoichiometric ratio and dissolved in water containing 3 ml of concentrated HNO_3. The above solution was stirred for about 1 h at room temperature. After 1 h of stirring, NH_4OH, NaOH and KOH solution was added dropwise, respectively. Here ammonia hydroxide, sodium hydroxide and potassium hydroxide were used as a reducing agent. The obtained brownish precipitate was filtered, washed with deionized water and dried at 80^0C overnight. Finally, the dried precursors were annealed at 600^0C for 2 h to obtain the required $BiFeO_3$ particles.

2.1 Systematic diagram

The photocatalytic degradation of organic molecules was investigated at room temperature with prepared semiconductor photocatalyst nanostructures in an aqueous solution. The reactor system (100 mL) comprises of photocatalyst (50 mg/L), target pollutant (200 mg/L), oxidants of ferrous sulfate heptahydrate (Fe_2SO_4 $7H_2O$, 1 mM) and hydrogen peroxide (H_2O_2, 20 mM). The pH of the above solution was adjusted with sulfuric acid (H_2SO_4, 2.5 M) and sodium hydroxide (NaOH, 2.5 M) under magnetic stirrer (200 rpm). Three parallel examinations such as UV light (254, 365 and 395 nm), visible light (300 W halogen lamp) and sunlight were carried out to determine the photocatalytic activities of the photocatalysts. The experimented solutions were pipetted out (3 mL) at sequence interval and measured the absorption at the wavelength of 354 nm after removed the photocatalyst by centrifugation (Scheme 1).

2.2 Characterization details

X-ray diffraction pattern of the synthesized sample was recorded on X'Pert Pro PANalytical diffractometer using Cu Kα radiation. The microstructure of the synthesized sample was studied using a Carl ZEISS scanning electron microscope. Ultra-violet visible spectrum study was carried out through the Shimadzu (Model: UV 2600). The electrochemical behavior was recorded using Sinsil instrument. The cell contains the three electrodes: (i) platinum electrode as secondary electrode, (ii) AgCl as a reference electrode and (iii) GCE (glassy carbon electrode) as working electrode.

2.3 Electrochemical characterization

The working electrode, $BiFeO_3$ (BFO1, BFO2, BFO3) nanoparticles were used as an active material. The active material was mixed in the proportion of 80:10:10 (80%—active material, 10%—polyvinylidene difluoride and 10%—carbon black) to form a slurry and coated over the working electrode (glassy carbon electrode). The mass of the active material pasted over the working electrode was 3 mg. This active electrode was then dried at 60 °C for 30 min. The electrochemical properties of nanoparticles were tested using a Sinsil three-electrode cell system in 0.1 M NaOH aqueous electrolyte. The experimental setup consisted of the active materials (3 mg), a platinum wire as secondary electrode and AgCl as reference electrode. The experiment was carried out at a potential range of − 1.5 to 1.5 V for different scan rates of 25, 50, 75, 100 mV/s.

Scheme 1: Systematic diagram of the synthesis process
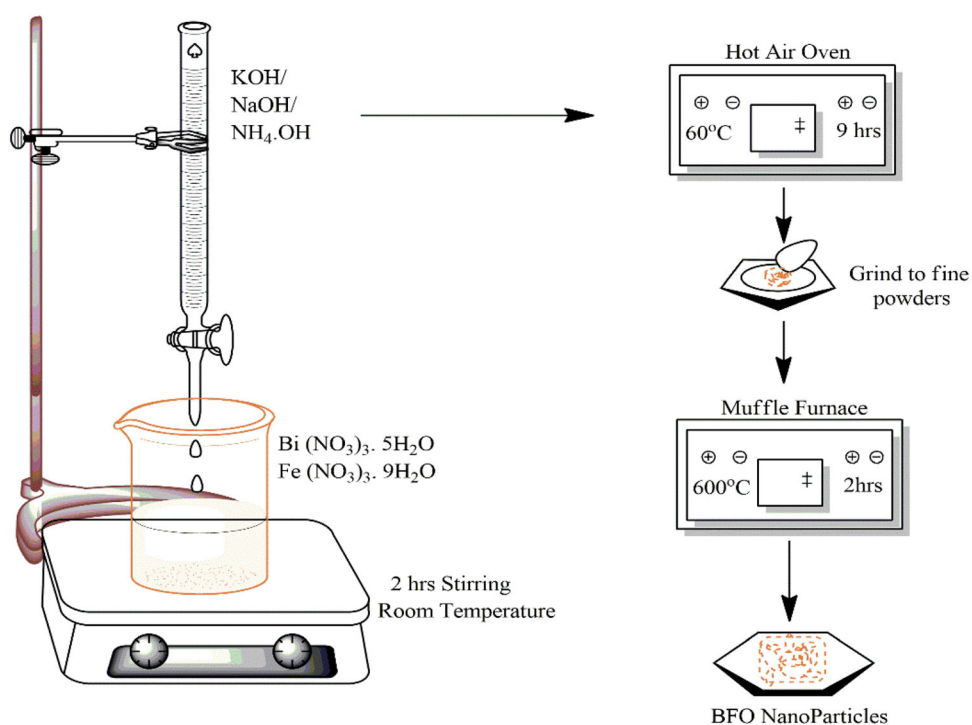
3 Results and discussion

3.1 XRD analysis

Being pH a major factor involved in the co-precipitation technique, the samples were synthesized using KOH as a reducing agent for different pH values 8, 10 & 12 to understand the optimum pH value for synthesizing a phase pure BFO. Figure 1a shows the XRD pattern of BFO synthesized for different pH which reveals that the sample synthesized at pH = 10 shows a good crystallinity and hinders the growth of the secondary phase ($Bi_2Fe_4O_9$ and $Bi_{25}FeO_{40}$) compared to pH = 8 & 12. Hence, the XRD pattern having a good agreement with the JCPDS data (No: 17-2494) pH = 10 seems to be an optimum condition for the chemical reaction to take place in producing phase pure BFO. Therefore, with a fixed parameter pH = 10 different reducing agents (NH_4OH, $NaOH$, KOH) were introduced to understand their effect on the compound formation. Figure 1b illustrates the BFO synthesized using NH_4OH, $NaOH$ and KOH, namely BFO1, BFO2 and BFO3, respectively. All three samples show a good agreement with the JCPDS No: 17-2494 having a rhombohedral distorted perovskite structure possessing an R3C space group without any secondary phases. But the observation of characteristic peak at 32° indicates that there is a change in their structural parameters leading to volume expansion [20–24]. These changes in unit cell parameters and volume were determined using unit

cell software tabulated [25, 26] in Table 1. Likewise, their particle size was determined using Debye Scherrer formula given in Eq. (1) [27], density using Eq. (2) and surface morphology index using Eq. (3) calculated and tabulated in Table 1 [27–29].

$$D = \frac{K\lambda}{\beta \cos\theta} \tag{1}$$

Here,

D is crystallite size, k is Scherrer's constant (0.9) [28], λ is the X-ray wavelength, β is the full width at half maximum (FWHM) [29], θ is the position of the Bragg diffraction angle

$$\rho = \frac{1.6609 \times M \times n}{a^2 \times c} \tag{2}$$

Here,

M is the molecular weight of $BiFeO_3$, n is the number of formula units in the unit cell taken as $n = 6$ for $BiFeO_3$, a and c are the lattice constants of the unit cell.

$$S = \frac{6 \times 10^3}{\rho D_p} \tag{3}$$

Here, S is the specific surface area, D_p is the size, and ρ is the density of $BiFeO_3$.

These results clearly illustrate that the type of reducing agent used in the synthesis influences over the compound formation, nature of the compound and property of the material.
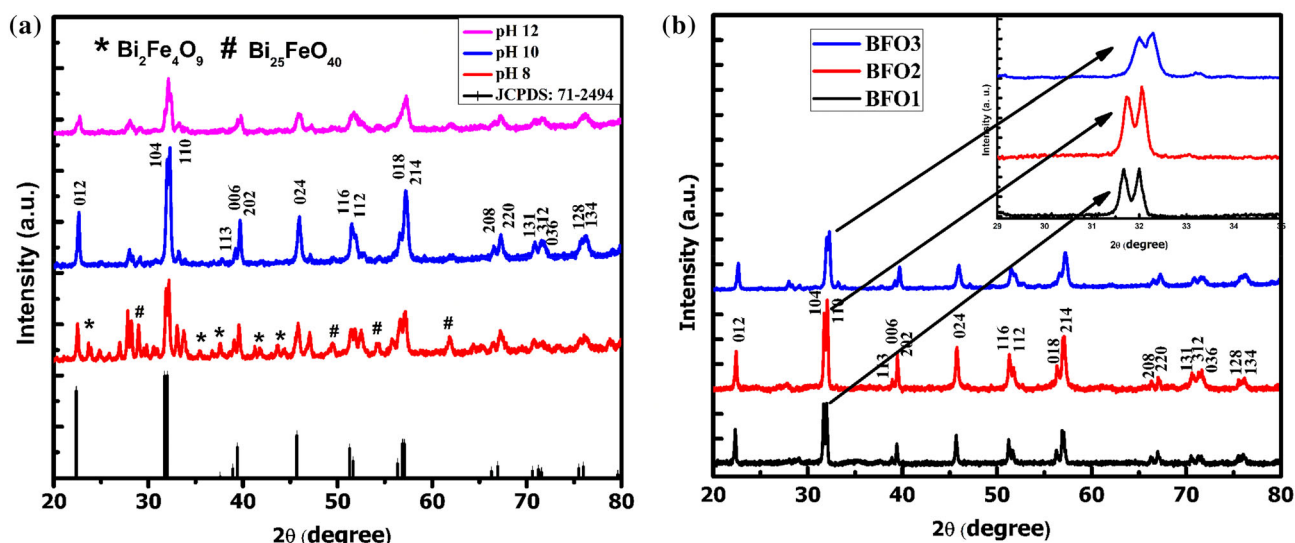

Fig. 1 **a** XRD pattern of synthesized $BiFeO_3$ for different pH values 8, 10, 12. **b** XRD pattern of $BiFeO_3$ synthesized using KOH, NaOH, and NH_4OH as reducing agents

3.2 UV spectra

In general, the absorption spectra were used to understand the optical property of the material. As the light incident on the sample, the electrons were energized leading to the transition in states. Figure 2a shows the UV absorption spectra of the synthesized samples. The excitation taking place at ~ 1.92 eV indicates the presence of d–d transition caused due to Fe^{3+} ion which is forbidden for the change in a total spin, but the relaxation in the spin selection rule led by the spin–orbital coupling gives rise to this transition [30, 31]. The other two charge transfer transitions around ~ 2.59 eV and ~ 3.4 eV were due to the intersite electron transfer and interatomic electron transfer between Fe 3d atoms and Fe 3d–O2p atoms, respectively. Also, the redshift of this transition goes following the XRD result that the shift may be caused due to the tilt in the octahedral environment (FeO_6) which is also a phenomenon explaining the reason for distortion of crystal structure [32–34]. Figure 2b shows the band gap values determined using Tauc's plot. The estimated band gap values were 2.18 eV,

2.18 eV, 2.12 eV for BFO1, BFO2 & BFO3, respectively. These results show that the tuning of optical bandgap can also be done using various reducing agent without altering the crystal system of the compound. Further to understand the structural property, Raman spectroscopy was carried out.

3.3 Raman spectroscopy

Figure 3 shows the Raman spectra of the synthesized samples. According to group theory, the material with R3C space group has 13 active modes $\Gamma_{Raman/IR} = 4A1 + 9E$. Here, the A1 modes take place due to Bi–O vibrations that normally occur in the region of lower frequencies up to 167 cm^{-1}, whereas the E(TO) modes are due to Fe–O vibration, which lies in the region of higher frequencies 152 cm^{-1}–262 cm^{-1} [35]. Since the ferroelectric and ferromagnetic behavior of BFO was employed by the Bi–O and Fe–O, respectively, the small variation in these values would reflect toward the property of the material. Usually the change in Bi–O covalent bonds

Table 1 Crystal size, volume, density, and specific surface area of the synthesized samples

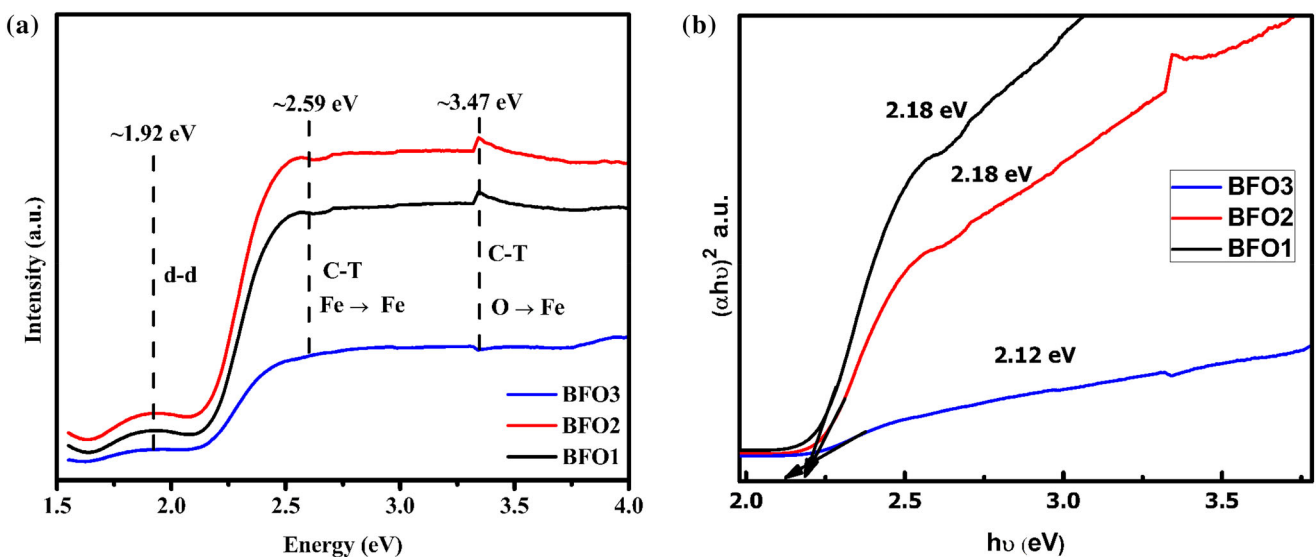| Sample	Crystallite size (nm)	Volume (m^3)	Density (g m^{-3})	SSA (m^2 g^{-1})
BFO1	31	375.87	7.195	26.90
BFO2	32	374.84	7.212	25.99
BFO3	42	373.83	7.227	19.76

Fig. 2 a Absorption spectrum of $BiFeO_3$ for BFO1, BFO2, and BFO3. **b** Shows the Bandgap for BFO1, BFO2, and BFO3 using Tauc's plot
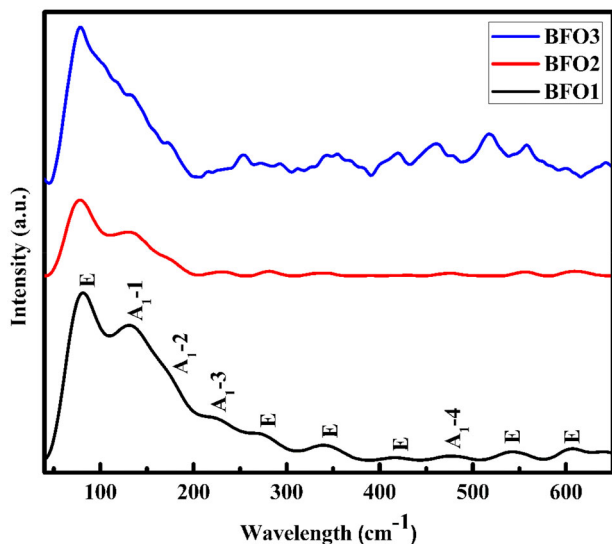
Fig. 3 Raman spectrum of BFO1, BFO2, and BFO3

observed in the A1, A2, A3, E1 and E2 modes takes place along c-axis which corresponds to the Bi lone pair electrons responsible for the ferroelectric property of BFO. Similarly, the changes in ferromagnetic behavior were caused by Fe–O1 mode at around 556 cm^{-1} and Fe–O2 mode at around 604 cm^{-1} along with the a and b-axis. These two modes E(TO) at 79 cm^{-1} and A1 at 130 cm^{-1} clearly show the displacement of lone pair electron in Bi. The suppression of A1 mode indicates the distortion in the unit cell without any structural transformation [36–39].

3.4 Microstructural analysis

Scanning electron microscopy was used to examine the shape of the synthesized nanomaterials. Figure 4a, b, c shows the morphology of BFO1, BFO2, BFO3 samples. It was found that all the samples were uniformly distributed and cuboid in shape.

3.5 Electrochemical studies

To study the contribution of the precipitant in the formation of BiFeO$_3$, the cyclic voltammetry studies were carried out and the results were found to be quite interesting that there is a remarkable change in the oxidation and reduction step in the redox reaction [40–42].

Figure 5a, b, c shows the cyclic voltametric graph explaining the redox reaction of BFO1, BFO2, BFO3. From the anodic peak, the changes in the oxidation of the elements present in the compound are addressable as shown in Fig. 6a, b, c. In comparing the compound BiFeO$_3$ made of NH$_4$OH, NaOH and KOH, we can conclude that the transition of Bi metal to Bi^{3+} state and Fe^{2+} to Fe^{3+} by losing the electron which is stable during the time of charging in NH$_4$-OH than compare toward the other two precipitants (NaOH and KOH) which exhibits a peak split during charging this phenomenon shows that there is no complete oxidation of Bi and Fe metals which would affect the charging of the material. From the cathodic peak, the changes in the reduction in the elements present in the compound are addressable. The transition of Bi metal to Bi^{3+} state and Fe^{2+} to Fe^{3+} by gaining the electron is stable during the time of discharging in NaOH and KOH when compared toward the NH$_4$OH which exhibits a peak split during discharging this phenomenon shows that there is no complete reduction of Bi and Fe metals which would lead to the longer duration of discharging which can benefit the battery applications.

Figure 7 shows the fit between peak current density vs scan rate of BFO1, BFO2 and BFO3, respectively. The linearity in the anodic peak current density (i$_{pa}$) and cathodic peak current density (i$_{pc}$) describes the electron transfer taking place in a controlled manner in BFO1 than compared to that of BFO2 and BFO3 which would significantly affect their specific capacitance value. Figure 7 shows the plot between scan rate vs specific capacitance. From the graph, we can observe that the BFO1 tends to have a higher specific capacitance value than BFO2 and BFO3 relatable to the current density behavior. Hence, through these analyses, it is clear that the NH$_4$OH is not only a suitable reducing agent but also has a better pseudo capacitance behavior. Due to this excellent electrochemical property exhibited by BFO1, it is further subjected to photocatalytic activity [43–45].

Figure 8a, b, c represents the EIS spectra of BFO1, BFO2, BFO3 revealing the charge transfer resistance of the samples. The sample having smallest semi-circle offers a lower charge transfer resistance
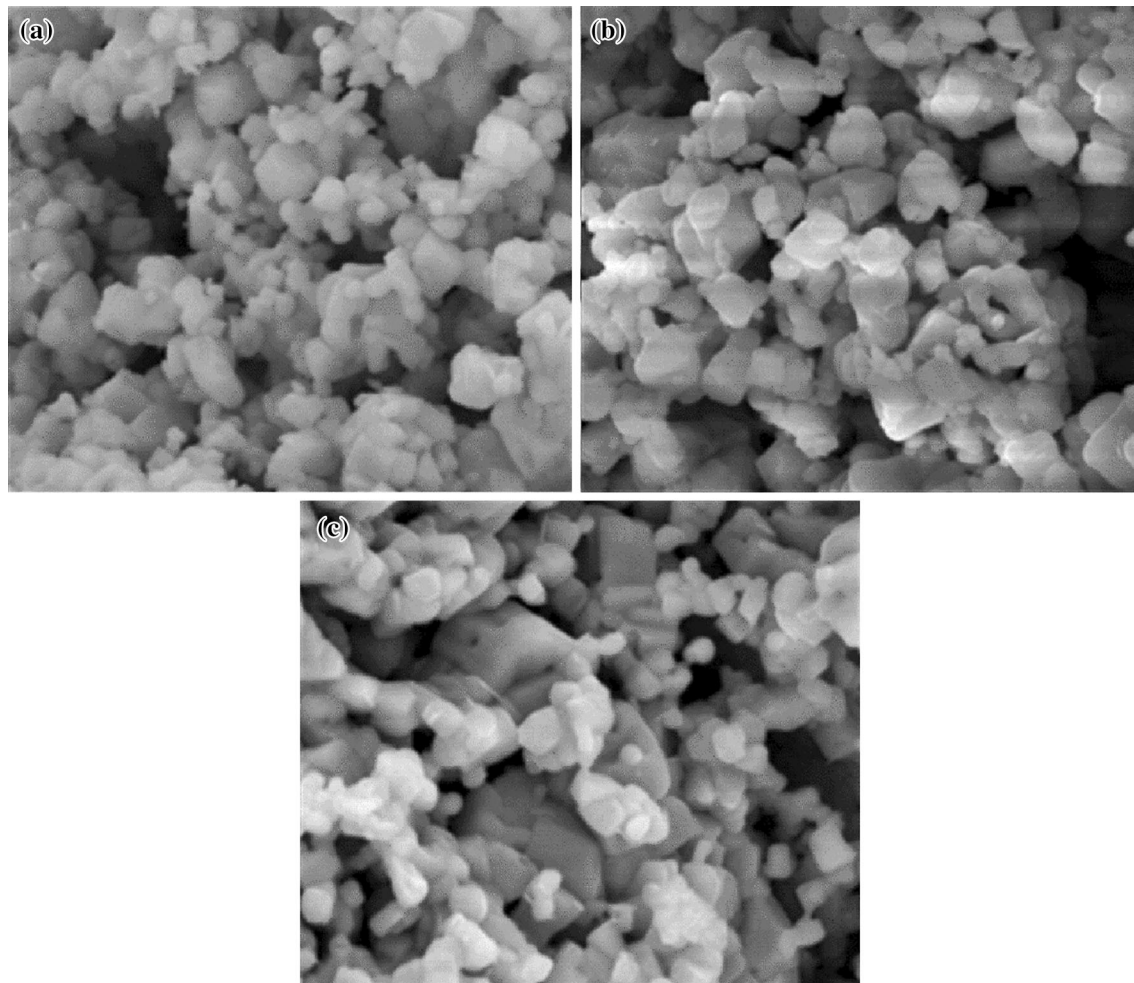
Fig. 4 Morphology of synthesized BFO1, BFO2 & BFO3 indexed as (**a**, **b**, **c**), respectively

benefiting the photocatalytic process. Hence, from the spectra BFO1 has a smallest semi-circle than BFO2, BFO3 which means BFO1 tends to have a better electron–hole charge carrier transportation for the effective degradation of pollutants. So, from the conclusion of these electrochemical behavior BFO1 sample was subjected to photocatalytic activity [46].

3.6 Photocatalytic activity

3.6.1 Photocatalytic performances under UV radiations

Figure 9a replicates the impact of pH (3–10) on the developed $BiFeO_3$–Fenton reagent's photocatalytic activity toward PA degradation under UV radiation

of 254 nm and links it to the result obtained from UV radiation of 365. The maximal rate of PA degradation (100%) was achieved at pH 3.0 (39 min), compared to pH 7.0 (61%) and 10.0 (51%) in that time, showing that an acidic medium is preferable for this degradation. It is envisaged that the partially negatively charged oxygen moiety of the PA molecule and the partially positively charged (protonated) surface of the $BiFeO_3$ will interact electrostatically to cause the degrading phenomena (Eq. 4). The $BiFeO_3$ valance band (VB) electrons are driven to the conduction band (CB) in addition to the Fenton processes, and when exposed to UV radiation, they create holes in the VB [47–49]. The superoxide radical ions $(O2-)$
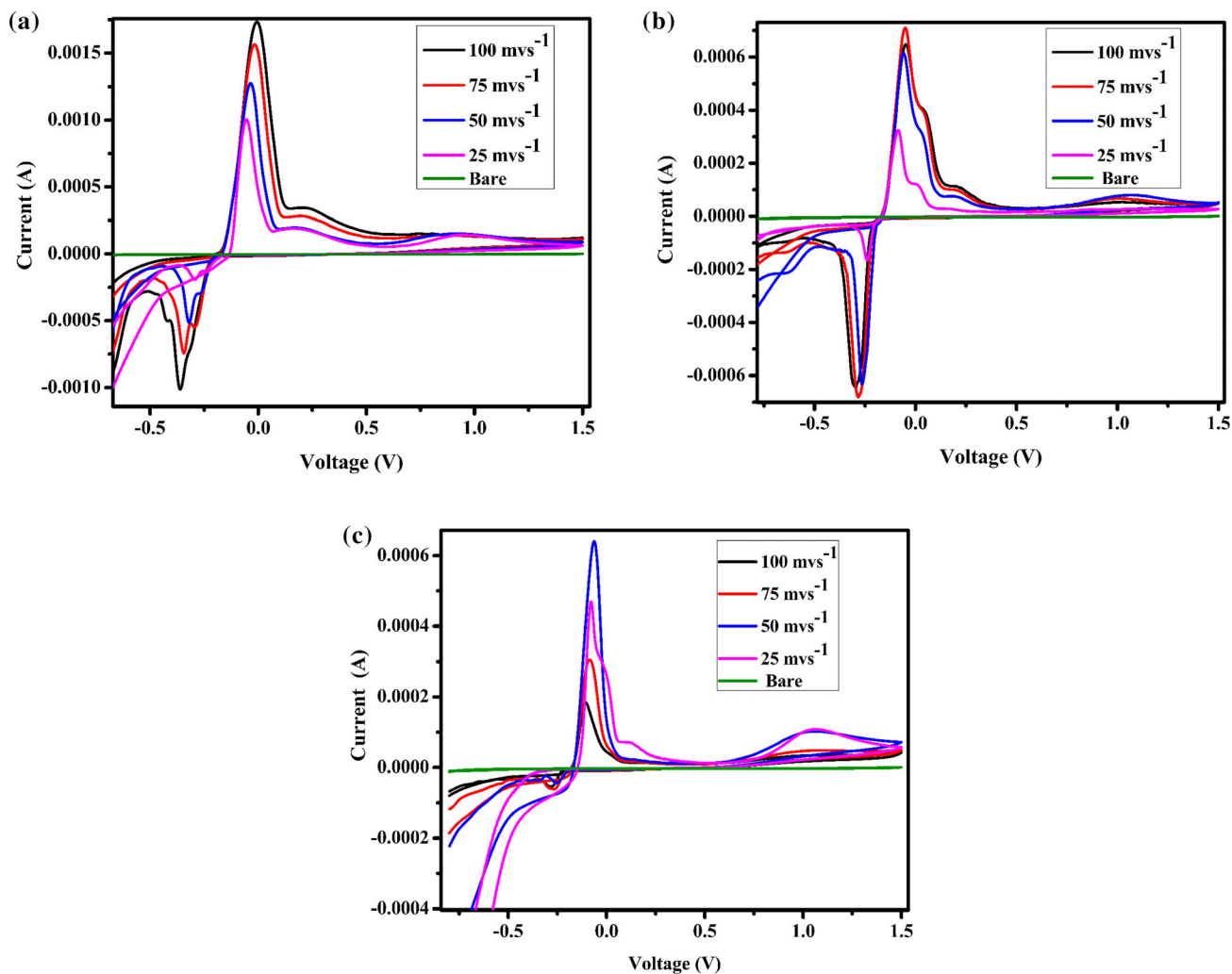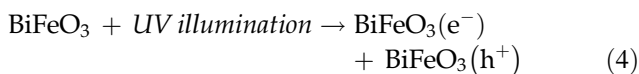
Fig. 5 a Redox reaction of BFO1. **b** Redox reaction of BFO2. **c** Redox reaction of BFO3

were produced by the reduction process between the excited electrons in CB and Fenton's reagent (Eq. 5). In the meantime, the VB holes directly oxidize organic pollutants or generate hydroxyl radicals (OH) (Eq. 6). The breakdown of the PA into the mild products is caused by the harvested radicals of O2 and OH. [50]. Owing to the negatively charged surface of BiFeO$_3$ nanoparticles, overall % degradation of the PA is slower at pH 7.0 and 10.0 than it is at pH 3.0.

$$BiFeO_3 + UV\ illumination \rightarrow BiFeO_3(e^-) \\ + BiFeO_3(h^+) \quad (4)$$

$$e^- + O_2 \rightarrow O_2^- \quad (5)$$

$$h^+ + H_2O_2 \rightarrow OH \quad (6)$$

Similar to this, Fig. 9b shows how the photocatalytic activity of PA has been expanded for the 365 UV rays. The properties of BiFeO$_3$-Fenton reagents are responsible for the trend's permanence as seen at 254 nm. Under acidic conditions, the UV radiation of 365 increased the maximal PA degradation rate by 36 min, respectively (pH 3.0). When compared to UV light at a wavelength of 254 nm, PA degradation was substantially same at pH values of 7.0 and 10.0. The photocatalytic degradation of picric acid at various
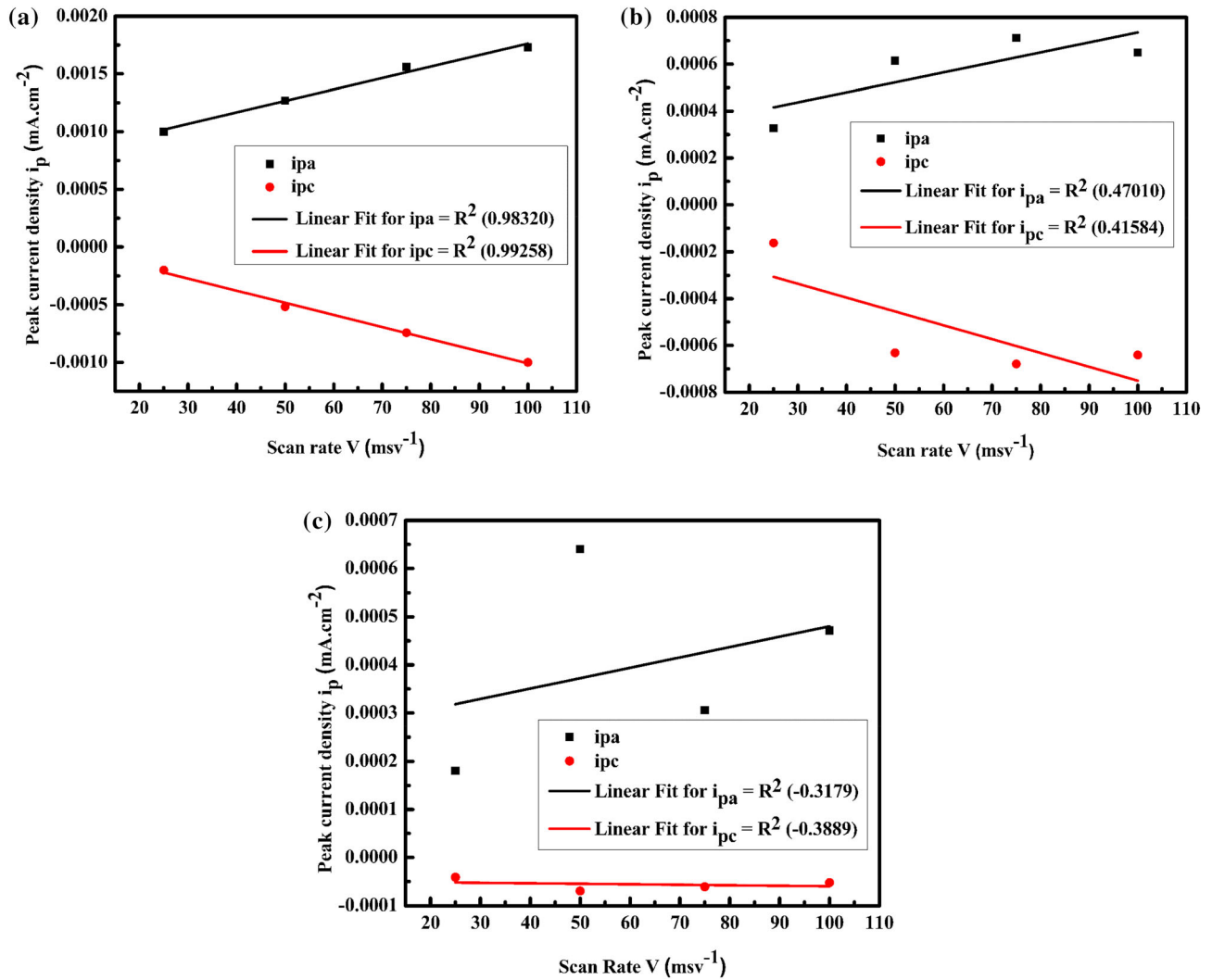
Fig. 6 **a** Anodic and cathodic peak current density of BFO1. **b** Anodic and cathodic peak current density of BFO2. **c** Anodic and cathodic peak current density of BFO3
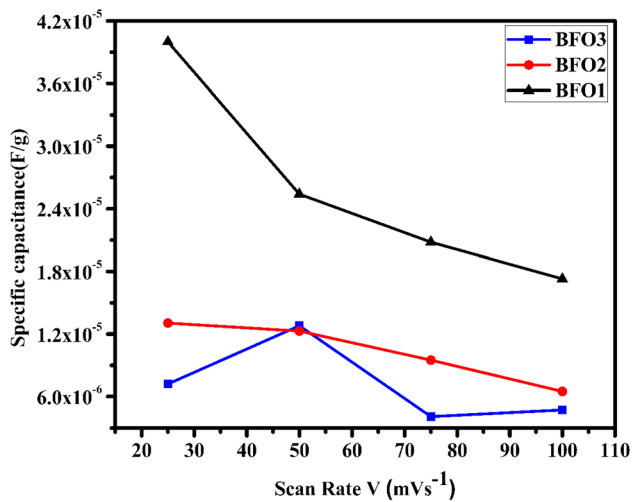

Fig. 7 Plot between scan rate vs specific capacitance

time intervals in the presence of $BiFeO_3$ (pH 3 and UV254) is represented in Fig. 9c.

Figure 10 depicts the degradation profiles of PA using various methods such as photo-Fenton catalyst (PFC, $BiFeO_3$-Fenton reagent), photocatalyst (PC, $BiFeO_3$), Fenton's reagent (F) and hydrogen peroxide (H_2O_2) under UV radiation of 254 nm (pH 4.0). It is clearly evident that the photodegradation efficiency of PA was found to be 100, 11, 37 and 27% for PFC-, PC-, F- and H_2O_2-based methods, respectively. It is indicating that Fenton's reagent encompasses with photocatalyst of $BiFeO_3$ possessed maximum activity toward PA degradation than other methods. As a result, the increased electron production of $BiFeO_3$-reagent Fenton's has influenced the free radicals
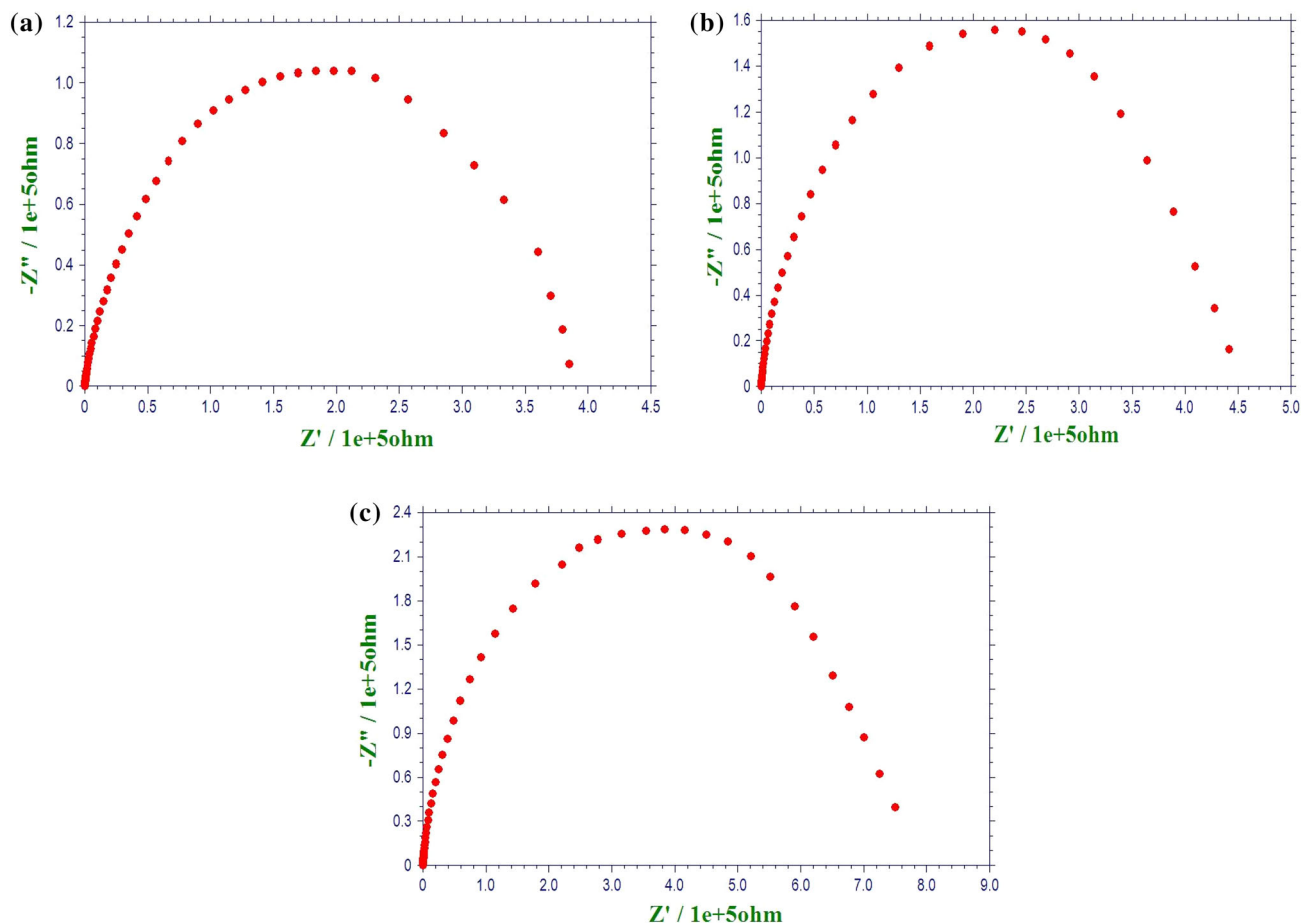
Fig. 8 a EIS spectra of BFO1 sample. **b** EIS spectra of BFO2 sample. **c** EIS spectra of BFO3 sample

responsible for PA mineralization in acidic suspensions.

3.6.2 Photocatalytic performances under visible light

The photocatalytic performance of the $BiFeO_3$-reagent Fenton's was also evaluated for the photodegradation of PA under visible light irradiation with the effect of pH (Fig. 11). The complete degradation was completed in 42 min for pH 3.0, which is significantly faster than the degradation achieved for pH 7.0 (60%, 42 min) and 10.0 (50 percent, 42 min). As a result, the same photo-Fenton reactions mechanism that was explained in the photodegradation by UV radiation could occur on the surface of the catalyst under visible light. A comparison table for BFO-based materials employed in photocatalytic activity is tabulated in Table 2.

3.6.3 Photocatalytic performances under sunlight

Figure 12 shows the results of an evaluation of the PA degradation efficiency with $BiFeO_3$ nanoparticles in a sunlight system using the same pH ranges. It eventually showed that the $BiFeO_3$ was photoactive even when exposed to sunlight. The PA was degraded to 100%, 61% and 56% by $BiFeO_3$ nanoparticles with pH values of 3.0, 7.0 and 10.0, respectively.
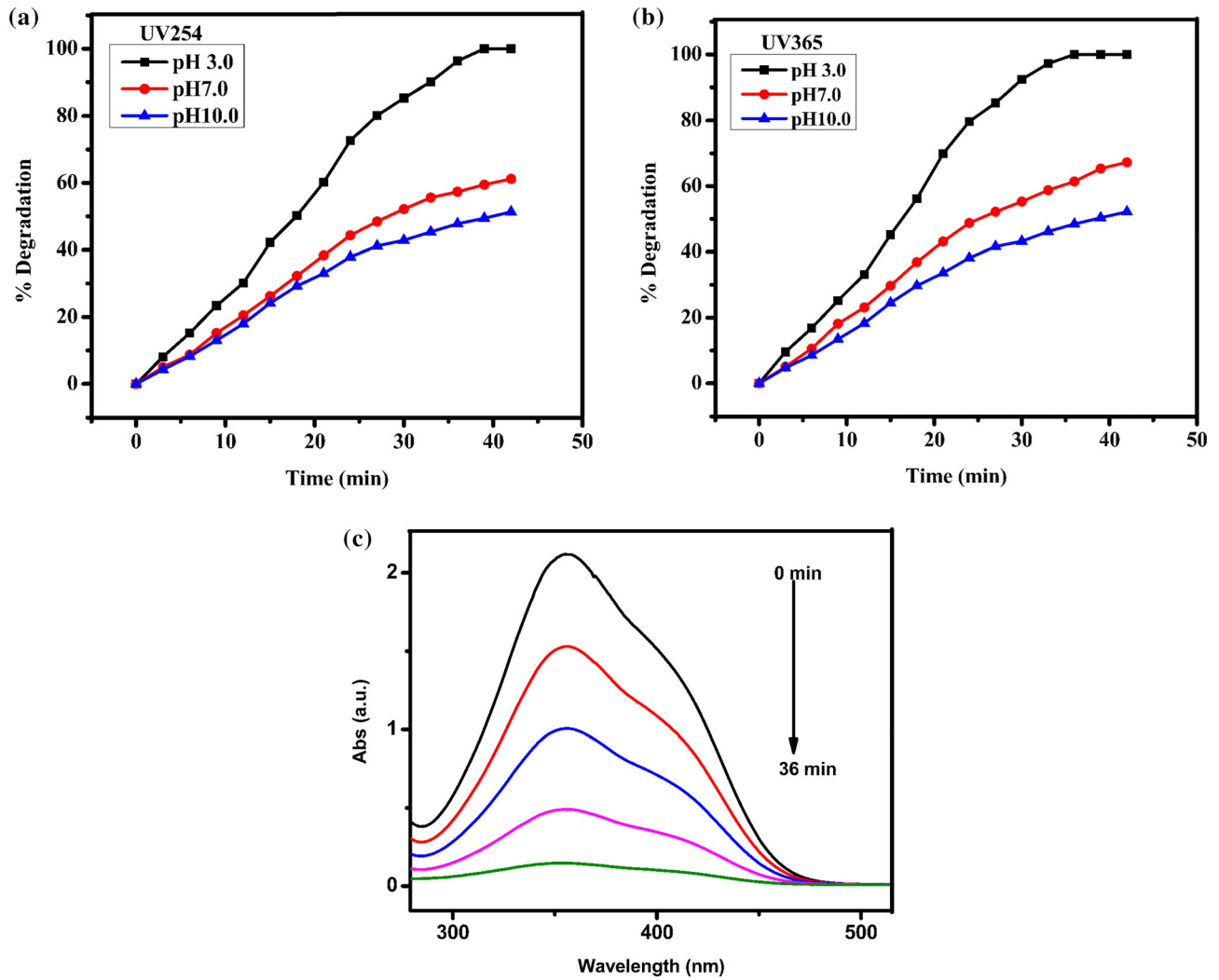
Fig. 9 a Photocatalytic activity of prepared BiFeO$_3$ toward the degradation of PA with effect of pH ranges from 3.0 to 10.0 under the UV radiation of 254 nm. **b** Photocatalytic activity of prepared BiFeO$_3$ toward the degradation of PA with effect of pH ranges from 3.0 to 10.0 under the UV radiation of 365 nm. **c** Photocatalytic degradation of picric acid at various time intervals in the presence of BiFeO$_3$ (pH 3 and UV254)

However, the degradation time of this reaction condition is extremely similar to that of the above-mentioned visible light reaction. As a result, inhibition efficiency for PA degradation in acidic medium is higher than in neutral and basic medium. Furthermore, UV illumination at 365 nm provided more accessible and effective results, and BiFeO$_3$ nanoparticles in combined application with Fenton's regent acted as an efficient photocatalysis toward PA degradation.
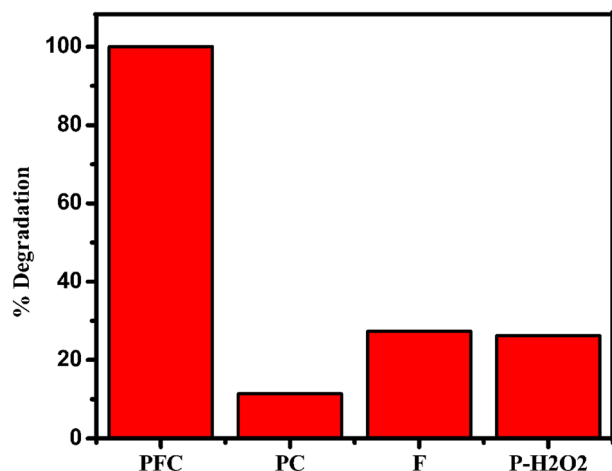
Fig. 10 Comparison studies of various methods under the UV 254 nm, (a) PFC photo-Fenton with catalyst, PC photocatalyst, F Fenton's process, and P-H_2O_2
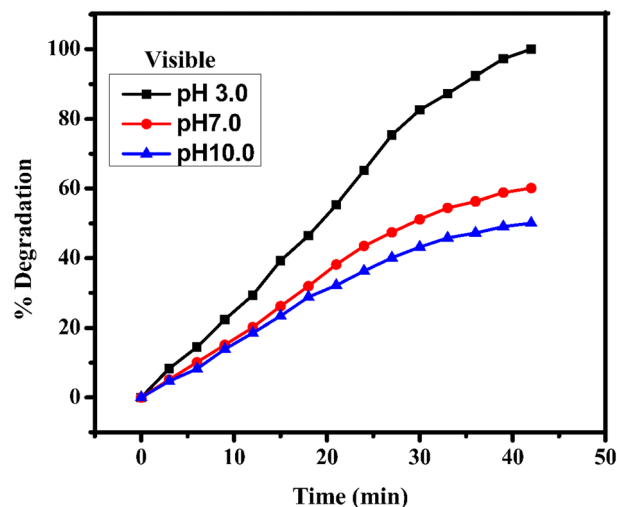

Fig. 12 Photocatalytic activity of prepared $BiFeO_3$ toward the degradation of PA with effect of pH ranges from 3.0 to 10.0 under the sunlight

4 Conclusion

From the above results and discussions, it is clear that the reducing agent is playing a vital role in not only the compound formation but also in the property of the materials. UV-spectrum shows the existence of d–d transition, C–T transition and tuning of band gap by reducing agent. Raman spectrum indicates the suppression of modes explaining the reason for structural distortion as per the XRD spectrum. Furthermore, photocatalytic activity of UV illumination at 365 nm, sun light, and UV all provided more accessible and effective results. Finally, $BiFeO_3$ nanoparticles acted as an efficient photocatalysis toward PA degradation when combined with Fenton's regent. Because it is uncommon to see catalysts active at all rays, it is advantageous to use Fenton-

Fig. 11 Photocatalytic activity of prepared $BiFeO_3$ toward the degradation of PA with effect of pH ranges from 3.0 to 10.0 under the visible light (300-W halogen lamp)
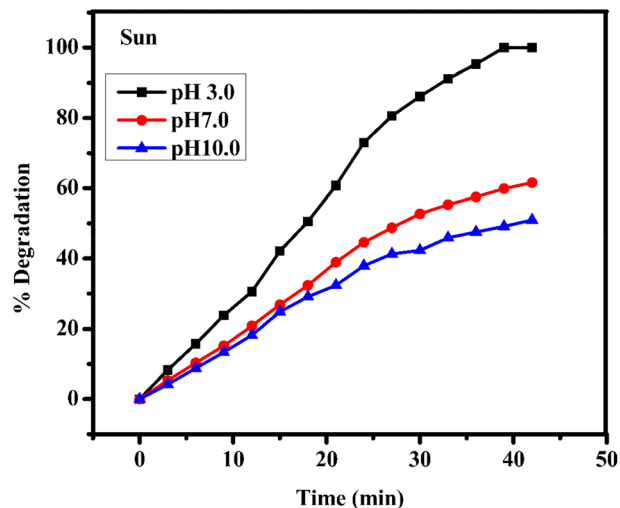
Table 2 Comparison of present work over the previously reported literatures

S. No	Materials	Dye	Degradation power (UV–Vis Light)	References
1	$BiFeO_3$	Rhodamine blue	66%(3 h)	[51]
2	La^{3+} doped $BiFeO_3$	Orange II dye	84.2%(2 h)	[52]
3	$BiFeO_3$	Malachite green	72.6%(4 h)	[53]
4	$BiFeO_3$	Picric acid	100%(36 min)	Present work

based multifunctionalized bismuth ferrite nanoparticles to degrade organic pollutants.

Author contributions

All authors contributed to the study conception and design. Material preparation, data collection, and analysis were performed by RMM, RDD, and PMYA. The first draft of the manuscript was written by RMM, RDD, and project administration SMAK, TS, supervision SMAK. All authors read and approved the final manuscript.

Funding

Data availability

The raw/processed data required to reproduce these findings cannot be shared at this time as the data also form part of an ongoing study.

Declarations

Competing interest The authors have no competing interests to declare that are relevant to the content of this article.

Ethical approval This is an observational study; no ethical approval is required.

Informed consent Not applicable.

Consent for publication Not applicable.

References

1. N.A. Spaldin, R. Ramesh, Advances in magnetoelectric multiferroics. Nat. Mater. **18**, 203–212 (2019). https://doi.org/10.1038/s41563-018-0275-2

2. A. Nicola Hill, Why are there so few magnetic ferroelectrics? J. Phys. Chem. B **104**, 6694–6709 (2000). https://doi.org/10.1021/jp000114x

3. S.M. Abdul Kader, D.E. Jain Ruth, M.V. Gajendra Babu, M. Muneeswaran, N.V. Giridharan, B. Sundarakannan, Investigations on the effect of Ba and Zr co-doping on the structural, thermal, electrical and magnetic properties of BiFeO$_3$ multiferroics. Ceram. Int. **43**, 15544–15550 (2017). https://doi.org/10.1016/j.ceramint.2017.08.104

4. J.C. Chen, W. Jenn-Ming, Dielectric properties and ac conductivities of dense single-phased BiFeO$_3$ ceramics. Appl. Phys. Lett. (2007). https://doi.org/10.1063/1.2798256

5. Y. Wang, X. Gang, Z. Ren, X. Wei, W. Weng, D. Piyi, G. Shen, G. Han, Low temperature polymer assisted hydrothermal synthesis of bismuth ferrite nanoparticles. Ceram Int **34**, 1569–1571 (2008). https://doi.org/10.1016/j.ceramint.2007.04.013

6. S. Ghosh, S. Dasgupta, A. Sen, H.S. Maiti, Low-temperature synthesis of nanosized bismuth ferrite by soft chemical route. J. Am. Ceram. Soc. **88**, 1349–1352 (2005). https://doi.org/10.1111/j.1551-2916.2005.00306.x

7. D.P. Dutta, A.K. Tyagi, Effect of Sm3+ and Zr4+ codoping on the magnetic, ferroelectric and magnetodielectric properties of sonochemically synthesized BiFeO$_3$ nanorods. Appl. Surf. Sci. **450**, 429–440 (2018)

8. M. Sakar, S. Balakumar, P. Saravanan, S.N. Jaisankar, Annealing temperature mediated physical properties of bismuth ferrite (BiFeO$_3$) nanostructures synthesized by a novel wet chemical method. Mater. Res. Bull. **48**, 2878–2885 (2013). https://doi.org/10.1016/j.materresbull.2013.04.008

9. N. Arpan Kumar, *Bismuth-Based Materials for Environmental Remediation* (IOP Publishing, 2022)

10. A. Puhan, B. Bhushan, S.S. Meena et al., Surface engineered Tb and Co co-doped BiFeO$_3$ nanoparticles for enhanced photocatalytic and magnetic properties. J Mater Sci: Mater Electron **32**, 7956–7972 (2021). https://doi.org/10.1007/s10854-021-05520-6

11. M. Muneeswaran, P. Jegatheesan, N.V. Giridharan, Synthesis of nanosized BiFeO$_3$ powders by co-precipitation method. J Exp. Nanosci. **8**, 341–346 (2011). https://doi.org/10.1080/17458080.2012.685954

12. M. Ismail, M.I. Khan, S.B. Khan, K. Akhtar, M.A. Khan, A.M. Asiri, Catalytic reduction of picric acid, nitrophenols and organic azo dyes *via* green synthesized plant supported Ag nanoparticles. J Mol Liq **268**, 87–101 (2018). https://doi.org/10.1016/j.molliq.2018.07.030

13. S. Senapati, K.K. Nanda, MgO nanocubes as self-calibrating optical probes for efficient ratiometric detection of picric acid in the solid state. ACS Sustain. Chem. Eng. **6**, 13719–13729 (2018). https://doi.org/10.1021/acssuschemeng.8b01330

14. A. Hakonen, F.C. Wang, P.O. Andersson, H. Wingfors, T. Rindzevicius, M.S. Schmidt, V.R. Soma, S. Xu, Y. Li, A. Boisen, H. Wu, Hand-held femtogram detection of hazardous picric acid with hydrophobic Ag nanopillar SERS substrates

and mechanism of elasto-capillarity. ACS Sens **2**, 198–202 (2017). https://doi.org/10.1021/acssensors.6b00749

15. R. Chakraborty, K. Vilya, M. Pradhan, A.K. Nayak, Recent advancement of biomass-derived porous carbon-based materials for energy and environmental remediation applications. J. Mater. Chem. A **10**, 6965–7005 (2022). https://doi.org/10.1039/D1TA10269A

16. A.K. Nayak, Nanostructured materials for visible light photocatalysis. Mater. Sci. Solid. **10**, 135–151 (2022)

17. N. Chnadel, K. Sharma, A. Sudahiak, P. Raizada, A. Hosseini-Bandegharaei, V. Thakur, P. Singh, Magnetically separable ZnO/ZnFe2O4 and ZnO/CoFe2O4 photocatalysts supported onto nitrogen doped graphene for photocatalytic degradation of toxic dyes. Arab J Chem (2019). https://doi.org/10.1016/j.arabjc.2019.08.005

18. V. Pawar, S. Gawande, An overview of the Fenton process for industrial wastewater. IOSR J Mech Civil Engg **2015**, 127–136 (2015)

19. F. Duan, Y. Ma, P. Lv, J. Sheng, L. Shuanglong, H. Zhu, D. Mingliang, X. Chen, M. Chen, Oxygen vacancy-enriched Bi_2O_3/$BiFeO_3$ p-n heterojunction nanofibers with highly efficient photocatalytic activity under visible light irradiation. Appl. Surf. Sci. **562**, 150171 (2021). https://doi.org/10.1016/j.apsusc.2021.150171

20. W. Xing, Y. Ma, Y. Bai, S. Zhao, Enhanced ferromagnetism of Er-doped $BiFeO_3$ thin films derived from rhombohedral-to-orthorhombic phase transformations. Mater. Lett. **161**, 216–219 (2015). https://doi.org/10.1016/j.matlet.2015.08.098

21. T.H. Le, N.V. Hao, N.H. Thoan, N.T.M. Hong, P.V. Hai, N.V. Thang, P.D. Thang, L.V. Nam, P.T. Tho, N.V. Dang, X.C. Nguyen, Origin of enhanced magnetization in (La, Co) codoped $BiFe_O3$ at the morphotropic phase boundary. Ceram. Int. **45**, 18480–18486 (2019). https://doi.org/10.1016/j.ceramint.2019.06.066

22. M. Rangi, S. Sanghi, S. Jangra, K. Kaswan, S. Khasa, A. Agarwal, Crystal structure transformation and improved dielectric and magnetic properties of La substituted $BiFeO_3$ multiferroics. Ceram. Int. **43**(2017), 12095–12101 (2017). https://doi.org/10.1016/j.ceramint.2017.06.065

23. D. Rout, M. Kyoung-Seok, L.K. Suk-Joong, Temperature-dependent Raman scattering studies of polycrystalline $BiFeO_3$ bulk ceramics. J. Raman Spectrosc. **40**, 618–626 (2009). https://doi.org/10.1002/jrs.2172

24. D. Singh, T. Tabari, M. Ebadi, M. Mateusz Trochowski, B. Yagci, W. Macyk, Efficient synthesis of $BiFeO_3$ by the microwave-assisted sol-gel method: "A" site influence on the photo electrochemical activity of perovskites. Appl. Surf. Sci. **471**(2019), 1017–1027 (2019). https://doi.org/10.1016/j.apsusc.2018.12.082

25. L. Hongping, L. Shuhui, W. Zhongchang, X. Yanjie, B. Yijia, L. Xiaojuan, M. Jian, Mechanism of A-B inter site charge transfer and negative thermal expansion in A-site ordered perovskite $LaCu_3Fe_4O_{12}$. J Appl Phys **111**, 103718 (2012). https://doi.org/10.1063/1.4721408

26. T. Durga Rao, T. Karthik, S. Asthana, Investigation of structural, magnetic and optical properties of rare earth substituted bismuth ferrite. J Rare Earths **31**, 370–375 (2013). https://doi.org/10.1016/S1002-0721(12)60288-9

27. P. Scherrer, Bestimmung der Grösse und der inneren Struktur von Kolloidteilchen mittels Röntgenstrahlen. Nachr. Ges. Wiss. Göttingen **26**, 98 (1918)

28. J.I. Langford, A.J.C. Wilson, Scherrer after sixty years: a survey and some new results in the determination of crystallite size. J. Appl. Cryst. **11**, 102 (1978)

29. V. Uvarov, I. Popov, Metrological characterization of X-ray diffraction methods for determination of crystallite size in nano-scale materials. Mater. Charac. **85**, 111 (2013)

30. R.V. Pisarev, A.S. Moskvin, A.M. Kalashnikova, Th. Rasing, Charge transfer transitions in multiferroic $BiFeO_3$ and related ferrite insulators. Phys. Rev. B **79**, 235128–235216 (2009). https://doi.org/10.1103/PhysRevB.79.235128

31. M.O. Ramirez, A. Kumar, S.A. Denev, N.J. Podraza, X.S. Xu, R.C. Rai, Y.H. Chu, J. Seidel, L.W. Martin, S.-Y. Yang, E. Saiz, J.F. Ihlefeld, S. Lee, J. Klug, S.W. Cheong, M.J. Bedzyk, O. Auciello, D.G. Schlom, R. Ramesh, J. Orenstein, J.L. Musfeldt, V. Gopalan, Magnon sidebands and spin-charge coupling in bismuth ferrite probed by nonlinear optical spectroscopy. Phys. Rev. B **79**, 224106–224109 (2009). https://doi.org/10.1103/PhysRevB.79.224106

32. S. Chaturvedi, R. Bag, V. Sathe, S. Kulkarnia, S. Singh, Holmium induced enhanced functionality at room temperature and structural phase transition at high temperature in bismuth ferrite nanoparticles. J Mater Chem C **4**, 780–792 (2016). https://doi.org/10.1039/C5TC02941D

33. G. Dong, G. Tan, Y. Luo, W. Liu, A. Xia, H. Ren, Charge defects and highly enhanced multiferroic properties in Mn and Cu co-doped $BiFeO_3$ thin films. Appl Surf Sci **305**, 55–61 (2014). https://doi.org/10.1016/j.apsusc.2014.02.159

34. R. Tadisetti Durga, S. Bhumireddi, A. Saket, Predicting high magneto-electric coupling in Gd substituted $BiFeO_3$. Phys. Status Solidi B **256**, 1900097–1900098 (2019). https://doi.org/10.1002/pssb.201900097

35. M. Muneeswaran, P. Jegatheesan, M. Gopiraman, N.V. Ick-Soo Kim, Giridharan, Structural, optical, and multiferroic properties of single phased $BiFeO_3$. Appl. Phys A **114**, 853–859 (2014). https://doi.org/10.1007/s00339-013-7712-5

36. S.K. Singh, H. Ishiwara, K. Maruyama, Room temperature ferroelectric properties of Mn-substituted $BiFeO_3$ thin films deposited on Pt electrodes using chemical solution deposition.

Appl. Phys. Lett. **88**, 262908–262913 (2006). https://doi.org/10.1063/1.2218819

37. J. Sharma, D. Basandrai, A.K. Srivastava, Ce Co-doped BiFeO$_3$ multiferroic for optoelectronic and photovoltaic applications. Chin. Phys. B **26**, 116201–116206 (2017). https://doi.org/10.1088/1674-1056/26/11/116201

38. R. Anlin Golda, A. Marikani, E. John Alex, Enhancement of dielectric, ferromagnetic and electrochemical properties of BiFeO$_3$ nanostructured films through rare earth metal doping. Ceram Int **46**, 1962–1973 (2020). https://doi.org/10.1016/j.ceramint.2019.09.175

39. J. Khajonrit, U. Wongpratat, P. Kidkhunthod, S. Pinitsoontorn, S. Maensiri, Effects of Co doping on magnetic and electrochemical properties of BiFeO$_3$ nanoparticles. J Magn Magn Mater **449**, 423–434 (2018). https://doi.org/10.1016/j.jmmm.2017.10.092

40. M. Kaur, P. Chand, H. Anand, Facile synthesis of NiCo$_2$O$_4$ nanostructure with enhanced electrochemical performance for supercapacitor application. Chem Phys Lett. **786**, 139181 (2022). https://doi.org/10.1016/j.cplett.2021.139181

41. M. Kaur, P. Chand, H. Anand, Effect of different synthesis methods on morphology and electrochemical behavior of spinel NiCo$_2$O$_4$ nanostructures as electrode material for energy storage application. Inorg. Chem. Commun. **134**, 108996 (2021). https://doi.org/10.1016/j.inoche.2021.108996

42. K.P. Remya, D. Prabhu, R. JustinJoseyphus, A. ChandraBose, C. Viswanathan, N. Ponpandian, Tailoring the morphology and size of perovskite BiFeO$_3$ nanostructures for enhanced magnetic and electrical properties. Mater. Design. **192**, 108694 (2020). https://doi.org/10.1016/j.matdes.2020.108694

43. H. Zhe, L. Wang, K. Zhang, J. Wang, F. Cheng, Z. Tao, J. Chen, MoS2 nanoflowers with expanded interlayers as high-performance anodes for sodium-ion batteries. Angew. Chem. Int. Ed. **53**, 12794–12798 (2014). https://doi.org/10.1002/anie.201407898

44. C.J. Ma, Y. Chen, C. Zhu, Q. Chen, W.L. Song, S. Jiao, H. Chen, D. Fang, Bismuth ferrite: an abnormal perovskite with electrochemical extraction of ions from A site. J. Mater. Chem. A **7**, 12176–12190 (2019). https://doi.org/10.1039/C9TA02569C

45. J. Zou, J. Jiang, Y. Zhang, J. Ma, Q. Wan, A comparative study of the optical, magnetic and electrocatalytic properties of nano BiFeO$_3$ with different morphologies. Mater. Lett. **72**, 134–136 (2012). https://doi.org/10.1016/j.matlet.2011.12.091

46. A. Sarkar, K. Gobinda Gopal, Synthesis of BiFeO$_3$ nanoparticle anchored TiO$_2$-BiFeO$_3$ nano hetero structure and

exploring its different electrochemical aspects as electrode. Mater. Today: Proc. **5**, 10177–10184 (2018). https://doi.org/10.1016/j.matpr.2017.11.016

47. Q. Wang, P. Wang, P. Xu, Y. Li, J. Duan, G. Zhanga, L. Hu, X. Wang, W. Zhang, Visible-light-driven photo-Fenton reactions using Zn$_{1-1.5x}$Fe$_x$S/g-C$_3$N$_4$ photocatalyst: degradation kinetics and mechanisms analysis. Appl Catal B Environ **266**, 118653 (2020). https://doi.org/10.1016/j.apcatb.2020.118653

48. P.K. Malik, S.K. Saha, Oxidation of direct dyes with hydrogen peroxide using ferrous ion as catalyst. Sep Purif Technol **31**, 241–250 (2003). https://doi.org/10.1016/S1383-5866(02)00200-9

49. Q. Wang, P. Xu, G. Zhang, W. Zhang, L. Hu, P. Wang, Characterization of visible-light photo-Fenton reactions using Fe-doped ZnS (Fe$_x$-ZnS) mesoporous microspheres. Phys Chem Chem Phys **20**, 18601–18609 (2018). https://doi.org/10.1039/c8cp02609b

50. M. Bhushan, R. Jha, R. Bhardwaj, Reduced band gap and diffusion controlled spherical n-type ZnS nanoparticles for absorption of UV-Vis region of solar spectrum. J Phys Chem Solids (2019). https://doi.org/10.1016/j.jpcs.2019.05.018

51. F. Mushtaq, X. Chen, M. Hoop, H. Torlakcik, E. Pellicer, J.S. Chiara Gattinoni, B.J. Nelson, S. Pané, Piezoelectrically enhanced photocatalysis with BiFeO$_3$ nanostructures for efficient water remediation. Iscience **4**, 236–246 (2018). https://doi.org/10.1016/j.isci.2018.06.003

52. O.V. Nkwachukwu, M. Charles, B.O. Ojo, B.N. Zwane, B.A. Koiki, B.O. Orimolade, D. Nkosi, N. Mabuba, O.A. Arotiba, Photoelectrochemical degradation of organic pollutants on a La^{3+} doped BiFeO$_3$ perovskite. Catalysts **11**(9), 1069 (2021). https://doi.org/10.3390/catal11091069

53. S.M. Lam, Z.H. Jaffari, J.C. Sin, A.R. Mohamed, IOP Conf. Series: Earth. Environ. Sci. **151**, 012021 (2018). https://doi.org/10.1088/1755-1315/151/1/012021